2 Discovery of a Dark Matter Decay Candidate Signal at 3.5 keV

2.1 Introduction

This Chapter will first present the discovery of a potential Dark Matter decay signal at 3.5 keV in the X-ray spectra of the Andromeda Galaxy (M31) and the Perseus Galaxy Cluster. All archival data taken with the *XMM-Newton* telescope for these objects is analyzed over the 2.8–8 keV range. This range avoids the most complicated parts of the spectrum that are crowded with emission or instrumental features. The central parts of Perseus are also avoided, size the cluster core environment is more complicated to model. After modeling, positive line-like residuals at 3.5 keV (restframe) are present in both objects. The possibility that the origin of this signal is an anomalously bright or previously undetected elemental emission line is investigated, but found implausible. In both objects the radial distribution of the signal strength is studied. These are consistent with expectations of Dark Matter decay, although the statistical strength is low upon splitting the data in radial bins. The relative strength of the signal between M31 and Perseus is also found to be consistent under a Dark Matter origin, within the (rather large) error bars. Lastly, a long-exposure blank-sky dataset is investigated in order to exclude an instrumental origin of the signal.

Secondly, an important consistency check is reported in the form of an analysis of the spectrum of the Galactic Center (GC). In archival *XMM-Newton* data of the GC, a feature at 3.5 keV is also found. The details of the spectral modeling are discussed, with special attention for the possibility that the signal originates with emission from Potassium or Argon ions. This interpretation can not be excluded for the GC, but neither is it neccesary that all of the 3.5 keV flux in the GC needs to be of elemental origin. This is mainly due to the extremely complicated and multi-component nature of the GC. The central premise of this work is therefore not to attempt to prove that one particular interpretation is correct, but rather whether one interpretation is *incorrect*. Based on the Dark Matter content of the GC, and given the fluxes and Dark Matter content of the objects considered previously (M31 and Perseus), it is possible to estimate the 3.5 keV line flux that is needed in the GC in order for the Dark Matter decay interpretation to remain valid. The conclusions of this work is that indeed, the Dark Matter origin remains a consistent and valid explanation.

The works considered here have been commented on by Jeltema & Profumo (2015). The comments regard a few subjects; firstly, the commenters' own analysis of the data of M31 does not show a feature at 3.5 keV. Secondly, it is claimed that in the analysis of the Perseus Cluster, and also in the analysis by Bulbul et al. (2014a), which reports a 3.5 keV signal in a stack of galaxy clusters, the 3.5 keV signal can be explained by Potassium and Chlorine emission lines. The last Section of this Chapter contains the response to the criticisms raised, finding that they are mostly unsupported, a conclusion which was later also supported by Bulbul et al. (2014b) and a similar argument being reproduced in Appendix 6.2.

2.2 Detection in the Andromeda Galaxy and Perseus Galaxy Cluster

BASED ON

An unidentified line in X-ray spectra of the Andromeda galaxy and Perseus galaxy cluster
Alexey Boyarsky, Oleg Ruchayskiy, Dmytro Iakubovskyi, Jeroen Franse
Published in *Physical Review Letters*

2.2.1 Data Analysis

We use the data obtained with MOS (Turner et al., 2001) and PN (Strüder et al., 2001) CCD cameras of *XMM-Newton* ("XMM" in what follows). We use SAS v.13.0.0[1] to reduce the raw data and filter the data for *soft solar protons* (Read & Ponman, 2003; Kuntz & Snowden, 2008) using the `espfilt` procedure. Because residual soft proton flares can produce weak line-like features in the spectra at positions where the effective area is non-monotonic (see e.g. Boyarsky et al., 2010b), we apply the procedure described in De Luca & Molendi (2004), based on the comparison of high-energy count rates for "in-FoV" (10-15 arcmin off-center) and out-FoV CCD regions[2]. We selected only observations where the ratio of $F_{in} - F_{out} < 1.15$.[3]

2.2.2 Analysis of M31

We use ~ 2 Msec of raw exposure observations of M31 within the central 1.5° (Tables 2.5 and 2.6). We select from the XMM archive 29 MOS observations offset less than $1.5'$ from the center of M31, and 20 MOS observations with offsets $23.7' - 55.8'$ that passed our criterion for residual contamination. Not enough PN observations passed this test to include them. The central and off-center observations were co-added seperately with the `addspec` routine from FTOOLS (Irby, B., 2008). The resulting spectra were binned by 60 eV. This bin size is a factor ~ 2 smaller than the spectral resolution of the XMM at these energies, which makes the bins roughly statistically independent.

We model the contribution of the instrumental (particle induced) background by a combination of an unfolded power law plus several narrow `gaussian` lines. The positions and normalizations of the lines were allowed to vary freely and the most prominent instrumental K-α lines (Cr, Mn, K, Fe, Ni, Ca, Cu) and Fe Kβ have been recovered. The width of the Gaussians was fixed at 1 eV (an infinitely thin line for the XMM spectral resolution). We verified that allowing the line widths to vary freely leaves the results unchanged. We restrict our modeling to the energy interval 2–8 keV. The Galactic foreground is negligible above 2 keV (Nevalainen et al., 2005). The combined emission of unresolved point sources at these energies is modeled by a `powerlaw` (Takahashi et al.,

[1] Xmm-newton science analysis system, http://xmm.esa. int/sas/

[2] Fin over fout public script, v. 1.1, `http://xmm.vilspa.esa.es/external/xmm_sw_cal/background/Fin_over_Fout`

[3] Ref. (De Luca & Molendi, 2004) argued that $F_{in} - F_{out} < 1.3$ is a sufficient criterion for flare removal. We find by visual inspection of the resulting spectra that a stricter criterion is needed to reduce artificial line-like residuals (Boyarsky et al., 2010b; Iakubovskyi, 2013). Lowering the threshold further is not feasible as the statistical errorbars on the value of $F_{in} - F_{out}$ are of the order of 5%.

Dataset	Exposure [ksec]	χ^2/d.o.f.	Line position [keV]	Flux $[10^{-6}\,\mathrm{cts/sec/cm^2}]$	$\Delta\chi^2$	Significance
M31 on-center	978.9	97.8/74	3.53 ± 0.03	$4.9^{+1.6}_{-1.3}$	13.0	3.2σ
M31 off-center	1472.8	107.8/75	$3.50 - 3.56$	$< 1.8\ (2\sigma)$	...	
Perseus (MOS)	628.5	72.7/68	3.50 ± 0.04	$7.0^{+2.6}_{-2.6}$	9.1	2.6σ
Perseus (PN)	215.5	62.6/62	3.46 ± 0.04	$9.2^{+3.1}_{-3.1}$	8.0	2.4σ
Perseus (MOS) + M31 on-center	1507.4	191.5/142	3.52 ± 0.02	$8.6^{+2.2}_{-2.3}$ (Perseus) $4.6^{+1.4}_{-1.4}$ (M31)	25.9 (3 dof)	4.4σ
Blank-sky	15700.2	33.1/33	$3.45 - 3.58$	$< 0.7\ (2\sigma)$	...	

Table 2.1: Basic properties of combined observations used in this paper. Second column denotes the sum of exposures of individual observations. The improvement in $\Delta\chi^2$ when extra line is added to a model is quoted for each dataset. The last column shows the local significance of such an improvement when 2 extra d.o.f. (position and flux of the line) are added. The energies for Perseus are quoted in the rest frame. Taking into account trial factors, the global (over three datasets) significance is 4.4σ (see Section 2.2.5.1 for details).

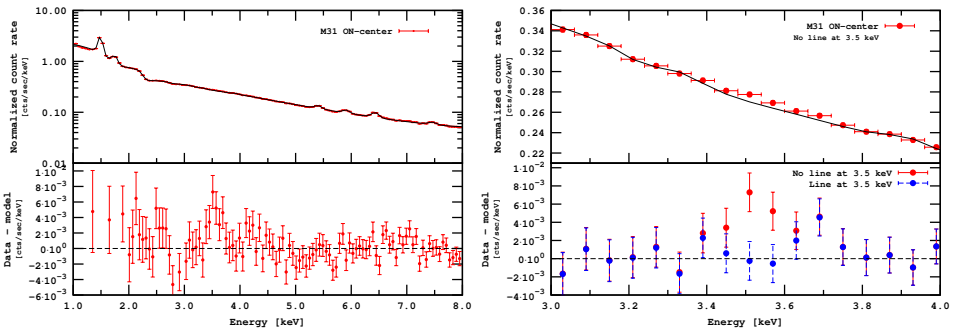

Figure 2.1: *Left:* Folded count rate (top) and residuals (bottom) for the MOS spectrum of the central region of M31. Statistical Y-errorbars on the top plot are smaller than the point size. The line around 3.5 keV is *not added*, hence the group of positive residuals. *Right*: zoom onto the line region.

2004). Several line-like residuals around 2.4 keV and 3.0 keV were identified as Ar and S line complexes and the corresponding thin (1 eV width) lines were added to the model. We verified that adding another `powerlaw` component to model the contribution of the extragalactic X-ray background (De Luca & Molendi, 2004; Nevalainen et al., 2005) does not improve the quality of fit and does not change the structure of the residuals.

The resulting spectrum of the central observations shows a group of positive residuals around 3.5 keV (Fig. 2.1). Adding a thin Gaussian line at that energy reduces the total χ^2 by ~ 13, see Table 2.1 (more than 3σ significance for extra 2 degrees of freedom). Examination of MOS1 and MOS2 observations individually finds the line in both cameras with comparable flux. For the off-center observations, none of the cameras show any detectable residual in the energy range $3.50 - 3.56$ keV. The 2σ upper bound on the flux is given in Table 2.1.

2.2.3 Perseus Cluster

If the candidate weak signal is of astrophysical (rather than instrumental) origin, we should be able to detect its redshift. To this end we have chosen the nearby Perseus cluster (Abell 426). At its redshift the line's centroid would be shifted by 63 eV. As the position of the line is determined with about 30 eV precision, one can expect to resolve the line's shift with about 2σ significance.

We took 16 off-center observations of the Perseus cluster (Table 2.3) and processed them in the same way as for M31. The flare removal procedure left 215 ksec of PN camera's exposure, therefore we also use PN data.

The resulting spectra were then added together and fitted to the combination of `vmekal` (with free abundances for Fe, Ni, Ar, Ca and S) plus (extragalactic) `powerlaw`. The instrumental background was modeled as in the M31 case.

The fit shows significant positive residuals at energies around 3.47 keV (in the detector frame). Adding a `zgauss` model with the redshift of the cluster improves the fit by $\Delta\chi^2 = 9.1$. The line's position is fully consistent with that of M31 (Table 2.1). If we fix the position of the line to that of M31 and allow the redshift to vary, $z = 0$ provides a worse fit by $\Delta\chi^2 = 3.6$ and its best-fit value is $(1.73 \pm 0.08) \times 10^{-2}$ – close to the value $z = 0.0179$ which we have used.

2.2.4 Interpretation

To further study the origin of the new line and possible systematic effects we combine XMM blank-sky observations from (Carter & Read, 2007; Henley & Shelton, 2012) with observations of the Lockman Hole (Brunner et al., 2008). The data were reduced similarly to the other datasets. Fig. 2.3 shows the combined spectrum. A dataset with such a large exposure requires special analysis (as described in (Iakubovskyi, 2013)). This analysis did not reveal any line-like residuals in the range $3.45 - 3.58$ keV with the 2σ upper bound on the flux being $7 \times 10^{-7}\,\mathrm{cts/cm^2/sec}$. The closest detected line-like feature ($\Delta\chi^2 = 4.5$) is at $3.67^{+0.10}_{-0.05}$ keV, consistent with the instrumental Ca Kα line.[4]

Finally, we have performed a simultaneous fit of the on-center M31 and Perseus datasets (MOS), keeping a common position of the line (in the rest-frame) and allowing the line normalizations to be different. The line improves the fit by $\Delta\chi^2 = 25.9$ – 4.4σ significance (Table 2.1).

We identified a spectral feature at $E = 3.52 \pm 0.02$ keV in the combined dataset of M31 and Perseus with a statistical significance 4.4σ which does not coincide with any known line. Next we compare its properties with the expected behavior of a DM decay line.

The observed brightness of a decaying DM should be proportional to its column density $S_{DM} = \int \rho_{DM} d\ell$ – integral along the line of sight of the DM density distribution –

[4]Previously this line has only been observed in the PN camera (Strüder et al., 2001).

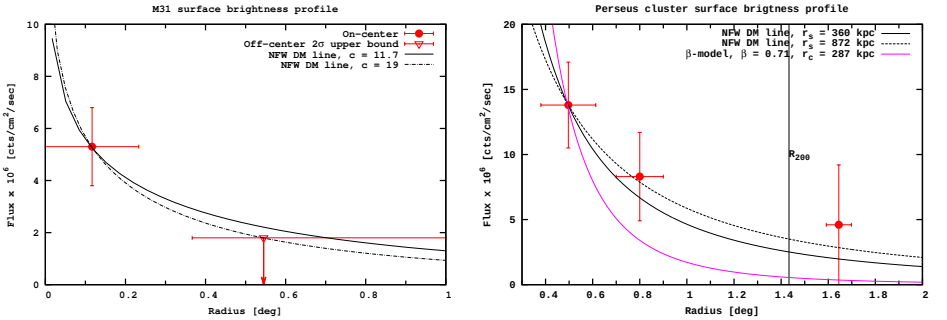

Figure 2.2: The line's brightness profile in M31 (left) and the Perseus cluster (right). A NFW DM distribution is assumed, the scale r_s is fixed to its best-fit values from Corbelli et al. (2010) (M31) or Simionescu et al. (2011) (Perseus) and the overall normalization is adjusted to pass through the left-most point.

and inversely proportional to the radiative decay lifetime τ_{DM}:

$$F_{DM} \approx 2.0 \times 10^{-6} \frac{\text{cts}}{\text{cm}^2 \cdot \text{sec}} \left(\frac{\Omega_{\text{fov}}}{500 \text{ arcmin}^2} \right) \times \left(\frac{S_{DM}}{500 \, \text{M}_\odot/\text{pc}^2} \right) \frac{10^{29} \text{ s}}{\tau_{DM}} \left(\frac{\text{keV}}{m_{DM}} \right). \tag{2.1}$$

Using the line flux of the center of M31 and the upper limit from the off-center observations we constrain the spatial profile of the line. The DM distribution in M31 has been extensively studied (see an overview in Boyarsky et al. (2010b)). We take NFW profiles for M31 with concentrations $c = 11.7$ (solid line, Corbelli et al. (2010)) and $c = 19$ (dash-dotted line). For each concentration we adjust the normalization so it passes through first data point (Fig. 2.2). The $c = 19$ profile was chosen to intersect the upper limit, illustrating that the obtained line fluxes of M31 are fully consistent with the density profile of M31 (see e.g. Corbelli et al., 2010; Chemin et al., 2009; Sánchez-Conde et al., 2011, for a $c = 19 - 22$ model of M31).

For the Perseus cluster the observations can be grouped in 3 radial bins by their off-center angle. For each bin we fix the line position to its average value across Perseus (3.47 ± 0.07 keV). The obtained line fluxes together with 1σ errors are shown in Fig. 2.2. For comparison, we draw the expected line distribution from DM decay using the NFW profile of Simionescu et al. (2011) (best fit value $r_s = 360$ kpc ($c \approx 5$), black solid line; 1σ upper bound $r_s = 872$ kpc ($c \approx 2$), black dashed line). The isothermal β-profile from Urban et al. (2014) is shown in magenta. The surface brightness profile follows the expected DM decay line's distribution in Perseus.

2.2.5 Discussion

Finally, we compare the predictions for the DM lifetime from the two objects. The estimated column density within the central part of M31 ranges between $\bar{S} \sim 200 - 1000 \, \text{M}_\odot/\text{pc}^2$ with the average value being around $600 \, \text{M}_\odot/\text{pc}^2$ (Boyarsky et al., 2010b).

The column density of clusters follows from the $c-M$ relation (Boyarsky et al., 2010a; King & Mead, 2011; Mandelbaum et al., 2008). Considering the uncertainty on the profile and that our observations of Perseus go beyond r_s, the column density in the region of interest is within $\bar{S} \sim 100 - 600\,\mathrm{M}_\odot/\mathrm{pc}^2$. Therefore the ratio of expected signals between Perseus and the center of M31 can be $0.1 - 3.0$, consistent with the ratio of measured fluxes $0.7 - 2.7$.

If DM is made of right-handed (sterile) neutrinos (Dodelson & Widrow, 1994), the lifetime is related to its interaction strength (*mixing angle*):

$$\tau_{DM} = \frac{1024\pi^4}{9\alpha G_F^2 \sin^2(2\theta) m_{DM}^5} = 7.2\times10^{29}\,\mathrm{sec}\left[\frac{10^{-8}}{\sin^2(2\theta)}\right]\left[\frac{1\,\mathrm{keV}}{m_{DM}}\right]^5.$$

Using the data from M31 and taking into account uncertainties in its DM content we obtain the mass $m_{DM} = 7.06 \pm 0.06$ keV and the mixing angle in the range $\sin^2(2\theta) = (2-20)\times10^{-11}$ (taking the column density $\bar{S} = 600\,\mathrm{M}_\odot/\mathrm{pc}^2$ and using only statistical uncertainties on flux we would get $\sin^2(2\theta) = 4.9^{+1.6}_{-1.3}\times10^{-11}$). This value is fully consistent with previous bounds, Fig. 2.4. Moreover, it is intriguing that this value is consistent with the result of Bulbul et al. (2014a), which appeared when our paper was in preparation. Indeed, our value of $\sin^2(2\theta)$ is based on completely independent analysis of the signal from M31 and our estimates for its DM content, whereas the result of Bulbul et al. (2014a) is based on the signal from stacked galaxy clusters and on the weighted DM column density from the full sample.

These values of $\sin^2(2\theta)$ means that sterile neutrinos should be produced resonantly (Shi & Fuller, 1999; Shaposhnikov, 2008; Laine & Shaposhnikov, 2008), which requires the presence of significant lepton asymmetry in primordial plasma at temperatures few hundreds MeV. This produces restrictions on parameters of the νMSM (Boyarsky et al., 2009c).

The position and flux of the discussed weak line are inevitably subject to systematical uncertainties. There are two weak instrumental lines (K Kα at 3.31 keV and Ca Kα at 3.69 keV), although formally their centroids are separated by more than 4σ. Additionally, the region below 3 keV is difficult to model precisely, especially at large exposures, due to the presence of the absorption edge and galactic emission. However, although the residuals below 3 keV are similar between the M31 dataset (Fig. 2.1) and the blank sky dataset (Fig. 2.3), the line is *not detected* in the latter.

If the feature were due to an unmodelled wiggle in the effective area, its flux would be proportional to the continuum brightness and the blank-sky dataset would have exhibited a 4 times smaller feature with roughly the same significance (see Section 2.2.5.2). In addition, the Perseus line would not be properly redshifted.

The properties of this line are consistent (within uncertainties) with the DM interpretation. To reach a conclusion about its nature, one will need to find more objects that give a detection or where non-observation of the line will put tight constraints on its properties. The forthcoming *Astro-H* mission (Takahashi et al., 2012) has sufficient spectral resolution to spectrally resolve the line against other nearby features and to detect the candidate line in the "strong line" regime (Boyarsky et al., 2007a). In particular, *Astro-H* should be able to resolve the Milky Way halo's DM decay signal and therefore all its observations can be used. Failure to detect such a line will rule out the DM origin of the Andromeda/Perseus signal presented here.

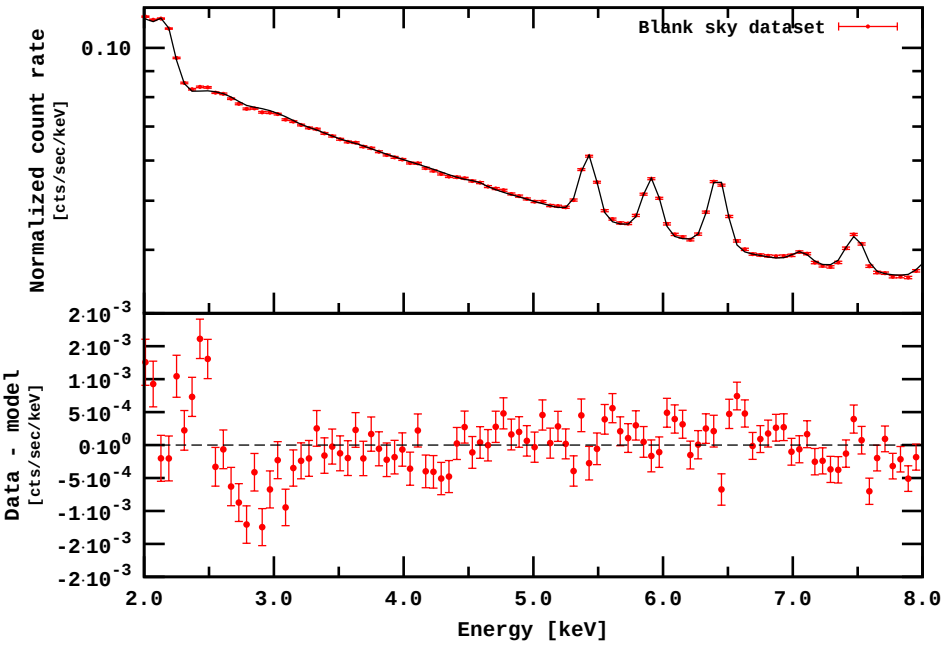

Figure 2.3: Combination of 382 MOS blank sky observations.

2.2.5.1 Global significance estimate

Significances quoted in the main body of the paper (Table 2.2) reflect the local significance of the signal. Since the position of the line is unknown *a priori* we need to take into account the probability of falsely detecting a statistical fluctuation of equal or higher significance at any position in the entire fitting range (2.0–8.0 keV). In addition, having found a signal in the same energy bin in three separate datasets, we compute this global significance taking into account the probability of such signals showing in the same resolution element by chance. Given the local significance of the signal in each dataset (based on the $\Delta\chi^2$ values and the number of degrees of freedom), and the number of independent resolution elements, we can determine the global significance of the combination of all signals. The number of independent resolution elements, N_E, for our datasets is about 40 (6 keV energy range divided by 150 eV — average energy resolution of the *XMM-Newton*).

The global significance per dataset is computed from the two-sided p-value p_i (directly related to the number of σ of the signal) by multiplying by N_E (see Table 2.2). We took a "two-sided" p-value to take into account both positive and negative residuals.

The combined global significance then is

$$\frac{\prod_i p_i N_E}{N_E^{N_d-1}} = 1.1 \cdot 10^{-5} \tag{2.2}$$

where $N_d = 3$ is the number of datasets. This corresponds to a false detection probability

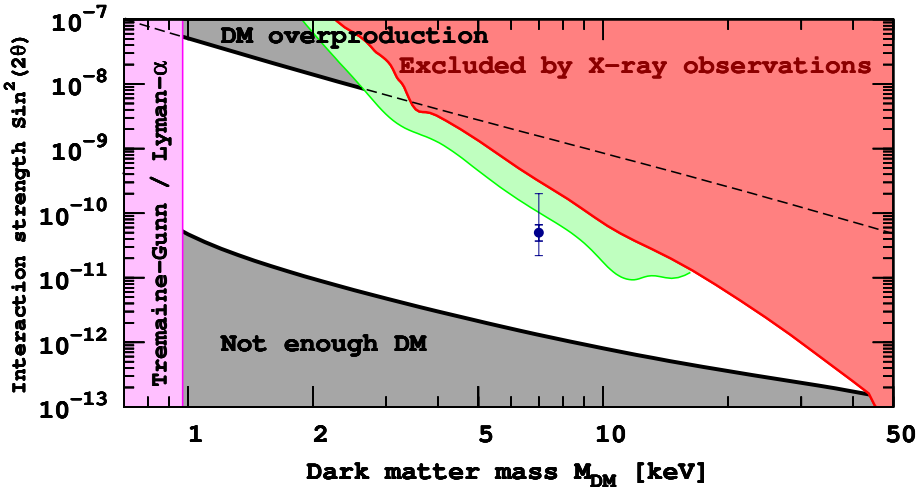

Figure 2.4: Constraints on sterile neutrino DM within νMSM (Boyarsky et al., 2012). Recent bounds from Watson et al. (2012); Horiuchi et al. (2014) are shown in green. Similar to older bounds (marked by red) they are smoothed and divided by factor 2 to account for possible DM uncertainties in M31. In every point in the white region sterile neutrino constitute 100% of DM and their properties agree with the existing bounds. Within the gray regions too much (or not enough) DM would be produced in a minimal model like νMSM. At masses below ~ 1 keV dwarf galaxies would not form (Boyarsky et al., 2009a; Gorbunov et al., 2008). The blue point would corresponds to the best-fit value from M31 if the line comes from DM decay. Thick errorbars are $\pm 1\sigma$ limits on the flux. Thin errorbars correspond to the uncertainty in the DM distribution in the center of M31.

Dataset	$\Delta\chi^2$	d.o.f.	local significance	local p-value	false detection probability	global significance
M31-oncen (MOS)	13	2	3.18σ	$1.5 \cdot 10^{-3}$	0.06	1.89σ
Perseus (MOS)	9.1	2	2.56σ	$1.05 \cdot 10^{-2}$	0.42	0.81σ
Perseus (PN)	8	2	2.36σ	$1.83 \cdot 10^{-2}$	0.73	0.35σ
All combined					$1.1 \cdot 10^{-5}$	4.4σ

Table 2.2: Table of significances per dataset. Quoted p-values refer to the two-sided case (one-sided p-values are half of the two-sided ones). The false detection probability refers to the probability of falsely detecting a signal in that dataset like the one under consideration or stronger at any energy in the range considered. The global significance was converted from the false detection probability per dataset. The combined false detection probability and global significance of these three datasets is also given (computed from the individual detections, not from a single combined dataset).

for the combination dataset of **0.0011%**. Converted to the significance this p-value gives 4.4σ **global significance**.

Alternatively, we could have taken into account only probability of positive fluctuations (so "two-sided" p-values in the Table 2.2 should be divided by 2). Using the same formula (2.2) we would obtain 4.7σ global significance.

Introducing systematic uncertainties into all our datasets at the level of $\sim 1\%$, the local significances drop by about 1σ each.

	ObsID	Off-axis angle arcmin	Cleaned exposure MOS1/MOS2 [ksec]	FoV [arcmin^2] MOS1/MOS2	F_{in}-F_{out}
1	0305690301	22.80	18.6 / 18.6	473.6 / 574.3	1.266 / 1.340
2	0085590201	25.01	40.1 / 40.5	564.6 / 572.1	1.290 / 1.336
3	0204720101	27.87	14.1 / 14.5	567.7 / 574.5	2.373 / 2.219
4	0673020401	29.48	15.6 / 17.6	479.6 / 574.0	1.318 / 1.331
5	0405410201	29.52	16.1 / 16.6	480.8 / 573.9	1.354 / 1.366
6	0305690101	29.54	25.1 / 25.4	476.0 / 573.5	1.231 / 1.247
7	0405410101	31.17	15.8 / 16.8	481.8 / 572.9	1.235 / 1.195
8	0305720101	31.23	11.5 / 11.8	476.8 / 573.9	1.288 / 1.296
9	0673020301	36.54	13.9 / 15.4	485.4 / 573.8	1.211 / 1.304
10	0305690401	36.75	25.9 / 26.0	479.1 / 573.8	1.158 / 1.156
11	0305720301	41.92	16.7 / 17.5	464.7 / 573.6	1.433 / 1.447
12	0151560101	47.42	23.7 / 23.6	572.1 / 573.6	1.294 / 1.206
13	0673020201	53.31	22.8 / 23.4	479.5 / 573.9	1.262 / 1.228
14	0204720201	54.11	22.4 / 22.9	564.0 / 573.2	1.153 / 1.195
15	0554500801	95.45	15.0 / 15.3	480.8 / 572.7	1.098 / 1.113
16	0306680301	101.88	12.3 / 13.0	468.1 / 574.0	1.177 / 1.089

Table 2.3: Parameters of the *XMM-Newton* spectra of the Perseus cluster used in our analysis. The observations are sorted by the off-axis angle from the center of the Perseus cluster. Two central observations (ObsIDs 0305780101 and 0085110101) were not included in the analysis to avoid modeling of the emission from the core of the Perseus cluster. Notice that only these two central observations were used in Boyarsky et al. (2008a), therefore that dataset and our dataset are independent from each other. The difference in FoVs between MOS1 and MOS2 cameras is due to the loss CCD6 in MOS1 camera. The parameter F_{in}-F_{out} (last column) estimates the presence of residual soft protons according to the procedure of http://xmm.vilspa.esa.es/external/xmm_sw_cal/background/Fin_over_Fout. Note, however, that for the bright extended sources, such an estimate is not appropriate, see http://xmm2.esac.esa.int/external/xmm_sw_cal/background/epic_scripts.shtml for details). Horizontal lines shows how we group observations for building the surface brightness profile of the line (as shown in Fig. 2, right panel).

Range of offsets	Exposure [ksec]	Flux [$\mathrm{cts/sec/cm^2}$]
$23 - 37'$	400	13.8 ± 3.3
$42' - 54'$	230	8.3 ± 3.4
$96' - 102'$	56	4.6 ± 4.6

Table 2.4: Definitions of the radial bins used for the data analysis of the Perseus cluster.

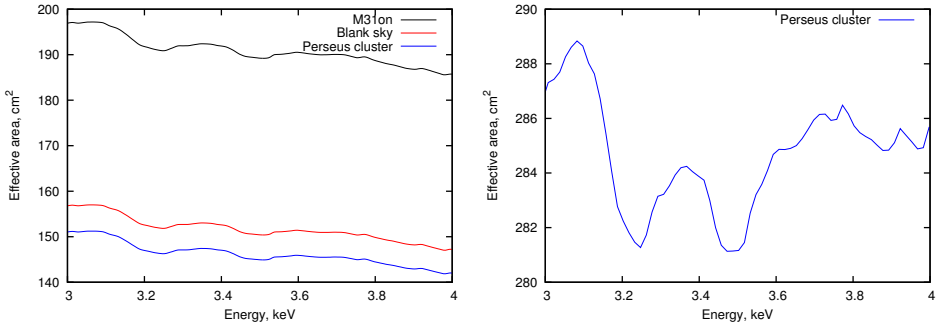

Figure 2.5: Exposure averaged effective area of the XMM MOS camera for the combination of observations of Perseus galaxy cluster, M31 and blank-sky (*left panel*). For Perseus galaxy cluster we also show the exposure averaged PN camera's effective area (*right panel*).

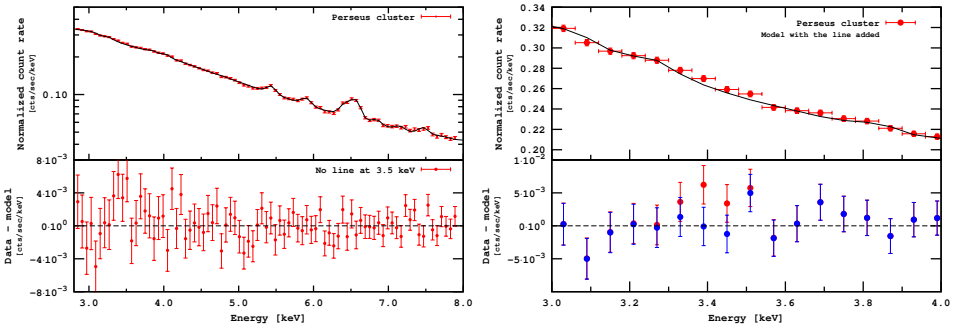

Figure 2.6: *Left:* Folded count rate (top) and residuals (bottom) for the combined spectrum of 16 observations of MOS cameras (listed in the Tabel 2.3) of the Perseus cluster. Statistical Y-errorbars on the top plot are smaller than the point size. The line around 3.5 keV is *not added*, hence the group of positive residuals. *Right*: zoom onto the line region. The spectrum is shown in the detector restframe, therefore the line is shifted left according to the Perseus redshift.

2.2.5.2 Effective area

In this Appendix we show the effective area of the Perseus, M31 and blank-sky datasets (Fig. 2.5). One sees that all three datasets exhibit a (known) wiggle at energy $E \sim 3.5$ keV in the detector frame (about 1.5% deviation from the monotonic behaviour). This kind of behavior of the effective area is due to K-, L- and M-shell transitions of Al, Sn and Au. The SAS software uses calibration files based on ray-tracing calculations through numerical models of the telescope assemblies (Gondoin et al., 2000; Turner et al., 2001; Strüder et al., 2001). The effective area curves differ between datasets mostly due to the vignetting effect, which depends on energy and on the weighting during the data stacking.

Looking at the left panel of Fig. 2.5 one sees that the effective area of all MOS observations is self-similar. The variation in shape between three datasets in the energy range 3.4-3.6 keV is less than 0.1% and less than 0.4% in the 3-4 keV range. If the line is due to an unmodeled wiggle, this would mean that a 10 times larger unmodeled feature (line

is 3-4% of the continuum level) is present in the datasets of M31 and Perseus, but *not* in the blank sky. As all datasets are combinations of observations taken over long period of lifetime of the XMM, the existence of such a feature is difficult to imagine.

Notice that if this wiggle would be the cause of the signal, reported in this paper, it would fail to explain why the redshift of the line in the Perseus cluster is correctly detected (at energies $3.5/1+z = 3.4$ keV the effective area has a local maximum, rather than minimum). It would also fail to explain the detection of the line in the combined dataset of 70 clusters at different redshifts, presented in Bulbul et al. (2014a).

Additionally, if the feature is due to an *unmodelled* wiggle in the effective area, its flux in each dataset should be proportional to the continuum brightness. Comparing the M31 and blank-sky datasets we see that the count rate at energies of interest is 4 times larger for M31, so that the blank-sky dataset would have exhibited a 4 times smaller (instrumental) feature with a flux $\sim 1.2\times 10^{-6}\,\mathrm{cts/sec/cm^2}$, were it due to a wiggle in the effective area. Notice that the exposure for the blank sky is 16 times larger and such a line would have been resolved with sufficient statistical significance. The upper (non-detection) limit from the blank-sky dataset is ~ 2 lower ($0.7\times 10^{-6}\,\mathrm{cts/sec/cm^2}$).

2.2.5.3 Flare removal

In this Section we investigate how sensitive the derived bounds are to the imposed $F_{in}-F_{out}$ cut. To this end we have imposed a number of different cuts in $F_{in}-F_{out}$ and rederived the 2σ upper bound in the blank sky dataset. We see (Fig. 2.7) that the bound derived in the paper does not really change until we start to impose very stringent cuts $F_{in}-F_{out}<1.06$, which starts to drastically reduce the statistics (clean exposure) as the blue squares in Fig. 2.7 demonstrate).

	ObsID	Off-axis angle arcmin	Cleaned exposure MOS1/MOS2 [ksec]	FoV [arcmin^2] MOS1/MOS2	F_{in}-F_{out}
17	0405320501	0.02	12.3/13.6	480.6/573.2	1.132/1.039
18	0405320701	0.02	14.8/14.9	480.7/572.8	1.046/1.057
19	0405320801	0.02	13.1/13.1	488.2/573.0	1.160/1.117
20	0405320901	0.02	15.5/15.6	488.0/574.3	1.099/1.065
21	0505720201	0.02	25.2/26.2	485.6/572.1	1.079/1.057
22	0505720301	0.02	25.4/24.3	486.0/573.9	1.129/1.105
23	0505720401	0.02	19.9/20.2	488.6/573.1	1.113/1.108
24	0505720501	0.02	12.9/13.9	480.3/574.1	1.151/1.064
25	0505720601	0.02	20.2/20.4	488.3/571.4	1.085/1.108
26	0551690201	0.02	20.5/20.3	486.5/574.2	1.099/1.072
27	0551690301	0.02	19.7/19.4	479.3/573.0	1.109/1.117
28	0551690501	0.02	16.9/18.4	486.3/573.2	1.095/1.109
29	0600660201	0.02	17.4/17.5	487.0/572.9	1.080/1.041
30	0600660301	0.02	16.1/16.1	488.6/572.0	1.054/1.041
31	0600660401	0.02	15.0/15.5	479.9/573.1	1.078/1.072
32	0600660501	0.02	13.5/14.3	488.2/573.4	1.079/1.083
33	0600660601	0.02	15.2/15.1	481.8/573.6	1.073/1.041
34	0650560201	0.02	21.0/21.3	488.1/573.3	1.198/1.140
35	0650560301	0.02	26.9/29.0	487.9/572.6	1.082/1.095
36	0650560401	0.02	12.4/13.5	488.0/573.1	1.157/1.069
37	0650560501	0.02	15.8/21.6	487.8/573.4	1.162/1.114
38	0650560601	0.02	20.8/21.5	487.5/572.2	1.085/1.068
39	0674210201	0.02	19.6/19.6	478.6/573.3	1.094/1.083
40	0674210301	0.02	14.9/15.0	488.1/573.6	1.052/1.043
41	0674210401	0.02	17.9/18.1	485.7/572.7	1.071/1.081
42	0674210501	0.02	16.2/16.3	488.8/573.5	1.192/1.139
43	0202230201	1.44	18.3/18.4	567.1/572.8	1.089/1.108
44	0202230401	1.44	17.0/17.1	566.5/573.6	1.118/1.109
45	0202230501	1.44	9.2/9.4	568.1/574.1	1.048/1.129

Table 2.5: Parameters of the *XMM-Newton* spectra of M31 used in our on-center analysis. The significant difference in FoVs between MOS1 and MOS2 cameras is due to the loss CCD6 in MOS1 camera. Off-center observations are found in Table 2.6.

	ObsID	Off-axis angle arcmin	Cleaned exposure MOS1/MOS2 [ksec]	FoV [arcmin^2] MOS1/MOS2	F_{in}-F_{out}
46	0402560201	23.71	16.0/16.6	478.7/574.0	1.096/1.095
47	0505760201	23.71	35.2/38.6	476.6/571.6	1.065/1.058
48	0511380201	23.71	15.3/15.4	485.0/572.7	1.126/1.047
49	0511380601	23.71	14.8/17.2	485.4/573.1	1.041/1.074
50	0402560901	24.18	42.4/42.9	475.0/572.8	1.118/1.071
51	0672130101	24.24	73.0/78.6	473.1/572.8	1.088/1.064
52	0672130501	24.24	22.7/25.4	477.0/574.8	1.097/1.110
53	0672130601	24.24	67.8/67.3	471.8/571.4	1.115/1.101
54	0672130701	24.24	70.7/74.3	484.8/573.5	1.076/1.052
55	0410582001	26.29	13.2/13.9	485.4/575.0	1.073/1.030
56	0402561001	28.81	48.0/49.4	478.4/572.5	1.084/1.042
57	0402560301	30.34	43.9/45.7	474.6/573.1	1.037/1.027
58	0505760301	39.55	41.0/41.3	485.0/570.8	1.022/1.022
59	0402561101	39.56	44.8/44.8	478.7/571.4	1.121/1.067
60	0404060201	42.94	19.1/19.1	480.7/573.7	0.993/1.045
61	0402561201	47.37	38.1/39.2	478.5/573.3	1.077/1.034
62	0402560501	49.06	48.8/50.6	487.2/572.9	1.102/1.079
63	0511380301	49.06	31.5/31.0	482.0/572.3	1.105/1.082
64	0151580401	50.89	12.3/12.3	567.2/574.1	1.131/1.020
65	0109270301	55.81	25.5/25.0	562.6/571.6	1.110/1.106

Table 2.6: Parameters of the *XMM-Newton* spectra of M31 used in our off-center analysis. The significant difference in FoVs between MOS1 and MOS2 cameras is due to the loss CCD6 in MOS1 camera. On-center observations are found in Table 2.5, and .

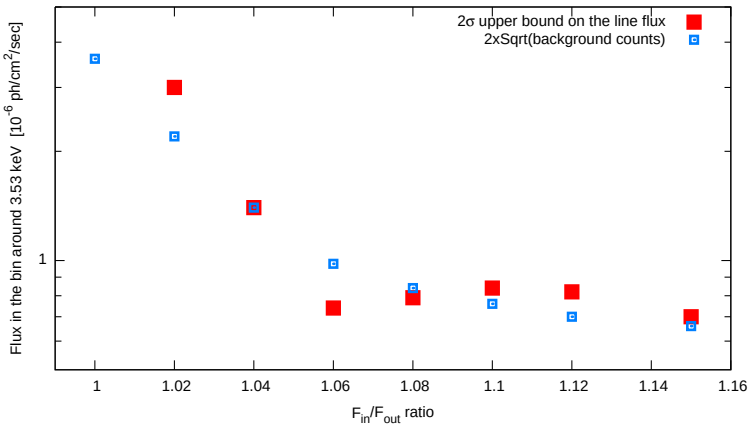

Figure 2.7: The dependence of the 2σ upper bound on the flux in the blanksky dataset on the imposed $F_{in} - F_{out}$ criterion. The statistical error on this parameter is about 5%. The bound on the flux remains at the quoted level until we start to lose significant fraction of observations for $F_{in} - F_{out} < 1.06$. Blue squares are defined as $2 \times \sqrt{N_{\rm bg}}$ where $N_{\rm bg}$ is the number of background counts in the energy bin, equal to spectral resolution. The difference between blue and red squares appears because spectral modeling trakes into account also the line shape.

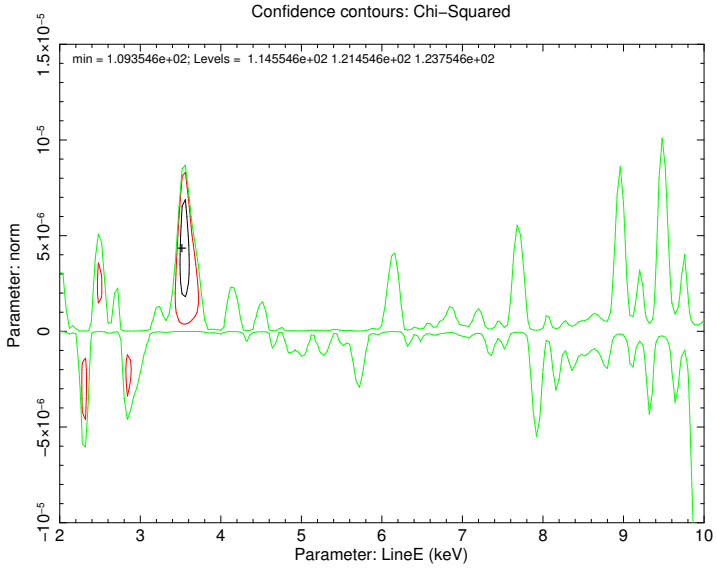

Figure 2.8: Structure of the residuals (both positive and negative) around the best fit model for M31 central observation. Red contours show residuals that are above 1σ. Black contour shows more than 3σ residual (3.53 keV line). The other residuals are below 1σ.

2.3 Detection in the Galactic Center

BASED ON
Checking the dark matter origin of 3.53 keV line with the Milky Way center
Alexey Boyarsky, Jeroen Franse, Dmytro Iakubovskyi, Oleg Ruchayskiy
Published in *Physical Review Letters*

2.3.1 Data and Analysis

We use all archival data of the Galactic Center obtained by the EPIC MOS cameras (Turner et al., 2001) with Sgr A* less than $0.5'$ from the telescope axis (see Table 2.7). The data are reduced by the standard `SAS`[5] pipeline, including screening for the time-variable soft proton flares by `espfilt`. We removed the observations taken during the period MJD 54000–54500 due to strong flaring activity of Sgr A* (see Fig. 2.11). The data reduction and preparation of the final spectra are similar to Section 2.2. For each reduced observation we select a circle of radius $14'$ around Sgr A* and combine these spectra using the `FTOOLS` (Irby, B., 2008) procedure `addspec`.

To account for the cosmic-ray induced instrumental background we have subtracted the latest closed filter datasets (Nevalainen et al. (2005)exposure: 1.30 Msec for MOS1 and 1.34 Msec for MOS2). The rescaling of the closed filter data has been performed such that the flux at energies $E > 10$ keV reduces to zero (see (Nevalainen et al., 2005) for details). We model the resulting physical spectrum in the energy range 2.8–6.0 keV. The X-ray emission from the inner part of the Galactic Center contains both thermal and non-thermal components (Kaneda et al., 1997; Muno et al., 2004). Therefore, we chose to model the spectrum with a thermal plasma model (`vapec`) and a non-thermal `powerlaw` component modified by the `phabs` model to account for the Galactic absorption.[6] We set the abundances of all elements – except for Fe – to zero but model the known astrophysical lines with `gaussians` (Bulbul et al., 2014a; Boyarsky et al., 2014a; Riemer-Sorensen, 2014). We selected the $\geq 2\sigma$ lines from the set of astrophysical lines of (Uchiyama et al., 2013; Bulbul et al., 2014a)[7]. The intensities of the lines are allowed to vary, as are the central energies to account for uncertainties in detector gain and limited spectral resolution. We keep the same position of the lines between the two cameras.

The spectrum is binned to 45 eV to have about 4 bins per resolution element. The fit quality for the dataset is $\chi^2 = 108/100$ d.o.f. The resulting values for the main continuum components – the folded `powerlaw` index (for the integrated point source contribution), the temperature of the `vapec` model ($\sim$8 keV), and the absorption column density – agree well with previous studies (Kaneda et al., 1997; Muno et al., 2004).

2.3.2 Results

The resulting spectra of the inner $14'$ of the Galactic Center show a $\sim 5.7\sigma$ line-like excess at 3.539 ± 0.011 keV with a flux of $(29 \pm 5) \times 10^{-6}\,\mathrm{cts/sec/cm^2}$ (see Fig. 2.9). It

[5] v.13.5.0 `http://xmm.esa.int/sas`

[6] The `Xspec` (Arnaud, 1996) v.12.8.0 is used for the spectral analysis.

[7] Unlike Bulbul et al. (2014a) we do not include K XVIII lines at 3.47 and 3.51 keV to our model. See the discussion below

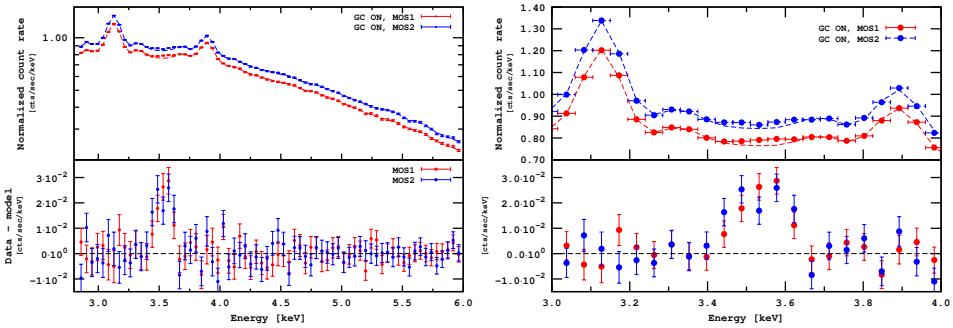

Figure 2.9: *Left:* Folded count rate for MOS1 (lower curve, red) and MOS2 (upper curve, blue) and residuals (bottom) when the line at 3.54 keV is *not added*. The difference between the cameras is due to detector gaps and bad pixels. *Right*: Zoom at the range 3.0–4.0 keV.

should be stressed that these 1σ error-bars are obtained with the `xspec` command `error` (see the discussion below). The position of the excess is very close to the similar excesses recently observed in Andromeda (3.53 ± 0.03 keV) and Perseus (3.50 ± 0.04 keV) reported in Boyarsky et al. (2014a), and is less than 2σ away from the one described in Bulbul et al. (2014a).

We also performed combined fits of the GC dataset with those of M31 and Perseus from Boyarsky et al. (2014a). As mentioned, the data reduction and modeling were performed very similarly, so we suffice with repeating that the inner part of M31 is covered by almost 1 Msec of cleaned MOS exposure, whereas a little over 500 ksec of clean MOS exposure was available for Perseus (see Section 2.2 for details).

We first perform a joint fit to the Galactic Center and M31, and subsequently to the Galactic Center, M31 and Perseus. In both cases, we start with the best-fit models of each individual analysis without any lines at 3.53 keV, and then add an additional gaussian to each model, allowing the energy to vary while keeping the same position between the models. The normalizations of this line for each dataset are allowed to vary independently. In this way, the addition of the line to the combination of Galactic Center, M31 and Perseus gives 4 extra degrees of freedom, which brings the joint significance to $\sim 6.7\sigma$.

To further investigate possible systematic errors on the line parameters we took into account that the `gaussian` component at 3.685 keV may describe not a single line, but a complex of lines (Table 2.8). Using the `steppar` command we scanned over the two-dimensional grid of this `gaussian`'s intrinsic width and the normalization of the line at 3.539 keV. We were able to find a new best fit with the 3.685 keV `gaussian` width being as large as 66 ± 15 eV. In this new minimum our line shifts to 3.50 ± 0.02 keV (as some of the photons were attributed to the 3.685 keV `gaussian`) and has a flux of 24×10^{-6} cts/sec/cm^2 with a 1σ confidence interval of $(13-36) \times 10^{-6}$ cts/sec/cm^2. The significance of the line is $\Delta\chi^2 = 9.5$ (2.6σ for 2 d.o.f.). Although the width in the new minimum seems to be too large even for the whole complex of Ar XVII lines (see 2.3.3), we treat this change of line parameters as the estimate of systematic uncertainties. To reduce these systematics one has either to resolve or to reliably model a line complex around 3.685 keV instead of representing it as one wide `gaussian` component.

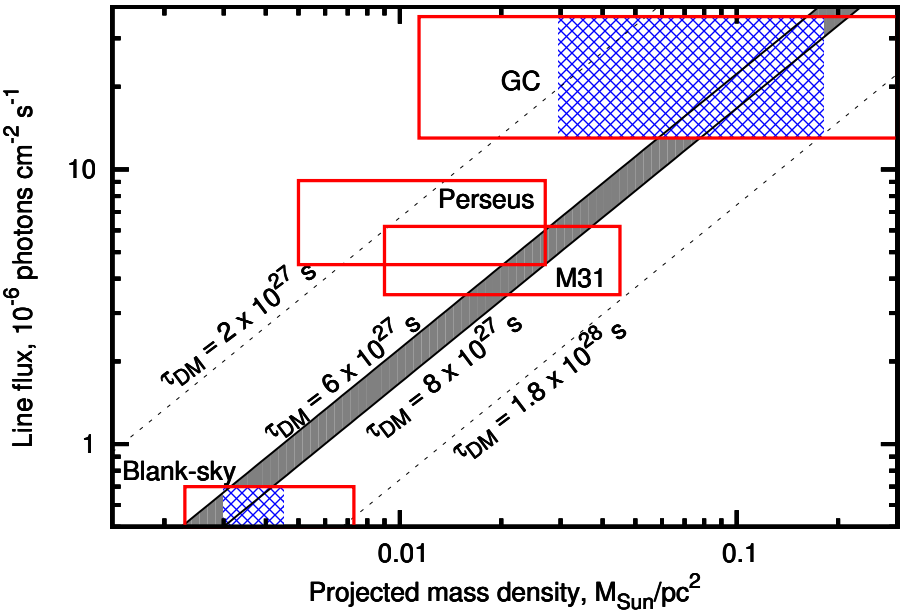

Figure 2.10: The flux of the 3.53 keV line in the spectra of the GC (this work), the Perseus cluster outskirts, M31 and the upper bound from blank sky (from Boyarsky et al. (2014a)) as a function of the mass within the XMM's field-of-view divided by the distance squared. Diagonal lines show the expected behaviour of a decaying DM signal for a given DM particle lifetime. The vertical sizes of the boxes are $\pm 1\sigma$ statistical error on the line's flux – or the 2σ upper bound for the blank-sky dataset. The horizontal sizes of the boxes represent systematic errors in the mass modeling by bracketing the literature values (see text). The Milky Way halo contribution to M31 is included (but not for Perseus, because the line is redshifted by $\sim$60 eV). As mentioned in the text, the distributions of the different objects are related to a greater or lesser extent, and the GC and blank-sky measurements in particular; the blue shaded regions give an example of this by showing one particular literature model of the Milky Way by Smith et al. (2007), its horizontal size indicating uncertainties in galactic disk modeling. This figure indicates that $\tau_{DM} \sim 6 - 8 \times 10^{27}$ sec is consistent with all datasets.

As was argued in Boyarsky et al. (2014a), an interpretation of the signal as an unmodelled wiggle in the effective area is not favoured because it should have produced a very significant signal in the blank-sky dataset as well. This is because an effect like this would produce a line-like residual proportional to the continuum level. In addition, the line would not be redshifted properly for Perseus (Boyarsky et al., 2014a) and the cluster stack from Bulbul et al. (2014a).

2.3.3 Discussion

In order to place this signal in context with respect to the DM interpretation of Bulbul et al. (2014a) and Boyarsky et al. (2014a), we need to compare the DM content of all relevant objects. A more detailed discussion of the following can be found in Section 2.3.4. We obtained literature DM distributions for Perseus, M31 and the MW. The latter applies

both to our GC results and the blank-sky upper limits. We are interested in the potential DM decay-product flux in each of our observations, and therefore require the detailed DM distributions rather than total mass. Any DM decay signal is expected to scale as the DM mass in the field-of-view divided by the distance squared to the DM, which we refer to as projected DM density. This quantity has a large uncertainty when we determine it from the literature distributions. The spread between the distributions is larger than the statistical errors quoted on the distribution parameters. For the GC, the case is even more complicated because there are no measurements of the DM distribution available within the inner 3 kpc, and they rely on extrapolating the distributions to small radii.

The situation is summarized in Fig. 2.10. It depicts all the measurements as a function of projected DM density against the expectations of a decaying DM scenario. This shows that a decaying DM with a lifetime of $\tau_{DM} \sim 6 - 8 \times 10^{27}$ sec would explain the signals from the GC, Perseus and M31, and the non-detection in the blank-sky dataset, given the uncertainties on the mass modeling. It should be noted that a correlation between the GC and blank-sky projected DM densities is necessarily present, since these are just different parts of the same halo; the blank-sky upper limit and the GC measurement require a cuspy DM profile. In addition, M31 and the Milky Way are expected to have (self)similar distributions, providing another consistency check. Boyarsky et al. (2014a) showed that in order to explain the signal from central $14'$ and non-observation from M31 outskirts, the Andromeda DM density profile should be cuspy, as predicted also for the Milky Way. This matter is also investigated using simulations in Lovell et al. (2015) and reports consistency of all measurements between objects as well. Lastly, in cluster outskirts the hydrostatic mass may be under-estimated (see e.g., Okabe et al., 2014), which would only improve the consistency between the data sets.

The non-detection of the signal in stacked dSphs by Malyshev et al. (2014) rules out the central values of the decay lifetime from Bulbul et al. (2014a) but is consistent with Boyarsky et al. (2014a) in case of large project DM mass (also preferred from comparison with other signals, Fig. 2.10). The signal was not detected in stacked galaxy spectra Anderson et al. (2015). However, the novel method of Anderson et al. (2015) has pronounced systematic effects (see their Appendix B) and is the least sensitive exactly at energies $E \sim 3.5$ keV. Iakubovskyi (2014) used a stacked dataset of nearby galaxies from Iakubovskyi (2013) and showed that systematic effects and uncertainty in dark matter distributions Boyarsky et al. (2010a) lead to the bound $\tau_{DM} \gtrsim 3.5 \times 10^{27}$ sec, consistent with our findings. Other bounds on decaying dark matter in the ~ 3.5 keV energy range (see Iakubovskyi (2013); Horiuchi et al. (2014); Sekiya et al. (2015) and references therein) are also consistent with our detections for lifetimes that we discuss in this work.

As mentioned in the Section 2.3.2, there is a degeneracy between the width of the Ar XVII complex around 3.685 keV and the normalization of the line in question. If we allow the width of the Ar XVII line to vary freely we can decrease the significance of the line at 3.539 keV to about 2σ. However, in this case the width of the `gaussian` at 3.685 keV should be $95 - 130$ eV, which is significantly larger than we obtain when simulating a complex of four Ar XVII lines wit the `fakeit` command. In addition, in this case the total flux of the line at 3.685 keV becomes *higher* than the fluxes in the lines at 3.130 and 3.895 in contradiction with the atomic data (Table 2.8).

Another way to decrease the significance of the line at 3.539 is to assume the presence

of a potassium ion (K XVIII) with a line at 3.515 keV and a smaller line at 3.47 keV. If one considers the abundance of potassium as a completely free parameter (as was done in Riemer-Sorensen (2014) for the Chandra data of the Galactic Center), one can find an acceptable fit of the XMM GC data without an additional line at 3.539 keV, for potassium abundances as low as $\sim$1 solar. As described in Section 2.3.5, due to the complicated internal temperature and abundance structures it is not possible to reliably constrain the overall potassium abundance of the GC to a degree that rules out the K XVIII origin of the 3.539 keV line *in this dataset*.

However, if we are to explain the presence of this line in the spectra by the presence of K XVIII, we have to build a model that consistently explains the fluxes in this line in different astronomical environments: in galaxy clusters (in particular Perseus) at all off-center distances from the central regions (Bulbul et al., 2014a) to the cluster outskirts up to the virial radius (Boyarsky et al., 2014a); in the central part of M31; and in the Galactic Center. In addition, we need to explain that this line is not observed – and therefore that this transition *should not* be excited – in the outskirts of the Milky Way and of M31 (Boyarsky et al., 2014a). Such a consistent model does not look convincing. In particular, in the case of M31 there are no strong astrophysical lines between 3 and 4 keV. The powerlaw continuum is well determined by fitting the data over a wider range of energies (from 2 to 8 keV) and allows a clear detection of the line at 3.53 ± 0.03 keV with $\Delta\chi^2 = 13$ (Boyarsky et al., 2014a), which is also the largest line-like feature in the entire 3–4 keV range. Were this signal in M31 due to K XVIII, there should be plenty of stronger emission lines present. In addition, the authors of Bulbul et al. (2014a) conclude that strongly super-solar abundances of K XVIII are required to explain the observed excess of this line in their stacked cluster analysis.

We conclude that although it is hard to exclude completely an astrophysical origin of the 3.539 keV line in the spectrum of the GC (due to the complicated nature of this object), the detection of this line in this object is an essential cross-check for the DM interpretation of the signal observed in Perseus and M31 (Boyarsky et al., 2014a) and in the stacked spectra of galaxy clusters (Bulbul et al., 2014a). A non-detection in the GC or a detection with a too high flux would have immediately ruled out this interpretation. As it is, the GC data rather supports this interpretation as the line is not only observed at the same energy, but also its flux is consistent with the expectations about the DM distribution of the GC.

To study this intriguing possibility further, a measurement with higher spectral resolution with respect to the atomic lines, an independent measurement of the relative abundances of elements in the GC region, or analyses of additional deep exposure datasets of DM-dominated objects are needed (Koyama et al., 2014; Lovell et al., 2015; Figueroa-Feliciano et al., 2015; Iakubovskyi, 2015; Speckhard et al., 2016).

	ObsID	Off-center angle arcmin	Cleaned exposure MOS1/MOS2 [ksec]	FoV [arcmin^2] MOS1/MOS2
1	0111350101	0.017	40.8/40.7	570.5/570.3
2	0111350301	0.017	7.2/6.8	565.8/573.4
3	0112972101	0.087	20.8/21.4	571.4/572.0
4	0202670501	0.003	21.4/26.5	564.9/573.4
5	0202670601	0.003	29.6/31.1	563.8/574.1
6	0202670701	0.003	76.0/80.0	570.4/573.3
7	0202670801	0.003	86.9/91.0	569.2/572.8
8	0402430301^a	0.002	57.6/60.2	475.8/572.1
9	0402430401^a	0.002	37.3/37.8	476.2/572.3
10	0402430701^a	0.002	23.1/25.2	478.5/573.1
11	0504940201^a	0.286	7.7/8.5	487.6/572.6
12	0505670101^a	0.002	65.7/73.7	472.0/573.2
13	0554750401	0.003	31.6/31.5	483.4/574.0
14	0554750501	0.003	39.6/39.2	487.0/574.0
15	0554750601	0.003	35.5/36.4	487.0/573.3
16	0604300601	0.003	28.9/30.0	487.1/573.1
17	0604300701	0.003	35.1/37.1	487.4/572.7
18	0604300801	0.003	34.9/34.2	487.8/572.5
19	0604300901	0.003	21.1/20.7	485.1/574.0
20	0604301001	0.003	35.3/38.6	487.4/573.6
21	0658600101	0.078	46.5/47.6	477.2/573.0
22	0658600201	0.078	38.3/39.7	478.3/572.3
23	0674600601	0.002	9.0/9.4	483.2/573.8
24	0674600701	0.003	12.8/13.5	484.9/575.0
25	0674600801	0.003	17.9/18.2	481.4/574.1
26	0674601001	0.003	20.0/21.5	480.9/573.7
27	0674601101	0.003	10.1/10.7	480.4/573.8

Table 2.7: Properties of the XMM observations of the Galactic Center used in our analysis. We have only used observations with centers located within 0.5' around Sgr A*. The difference in FoVs between MOS1 and MOS2 cameras is due to the loss CCD6 in MOS1 camera, see (Abbey et al., 2006) for details.
^{a} Observation discarded from our analysis due to flares in Sgr a*, see Fig. 2.11 and (Porquet et al., 2008).

2.3.4 Dark Matter Profiles of the Milky Way

The distribution of dark matter in galaxies, galaxy groups and galaxy clusters can be described by several density profiles. In this work we concentrated on four popular choices for dark matter density profiles.

I. Numerical (N-body) simulations of the cold dark matter model have shown that the dark matter distribution in all relaxed halos can be fitted with the universal Navarro-Frenk-White (NFW) profile (Navarro et al., 1997)

$$\rho_{\rm NFW}(r) = \frac{\rho_s r_s}{r(1+r/r_s)^2} \tag{2.3}$$

parametrised by ρ_s and r_s.

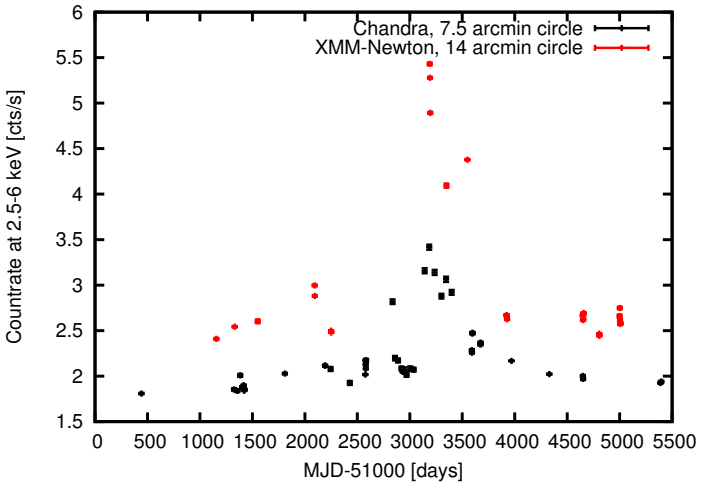

Figure 2.11: Average count rates on regions centered in Sgr a* using *XMM-Newton* (red) and *Chandra* (black). The enhancement at MJD 54000-54500 are due to strong flaring activity of Sgr a*, see (Porquet et al., 2008) for details. 5 *XMM-Newton* observations during this flaring period were discarded from our analysis, see Table 2.7 for details.

Ion	Position keV	Upper level	Lover level	Emissivity ph cm^3 s^{-1}	T$_e$ peak keV	Relative intensity
Ca XIX	3.902	7	1	3.913e-18	2.725e+0	0.59
Ca XIX	3.883	5	1	6.730e-19	2.725e+0	0.10
Ca XIX	3.861	2	1	1.242e-18	2.165e+0	0.19
Ar XVII	3.685	13	1	8.894e-19	1.719e+0	0.13
Ar XVII	3.683	11	1	3.729e-20	1.719e+0	0.01
Ar XVII	3.618	10077	2	3.627e-20	1.366e+0	0.01
Ar XVII	3.617	10078	3	9.355e-20	1.366e+0	0.01
Ar XVIII	3.323	4	1	4.052e-18	3.431e+0	0.61
Ar XVIII	3.318	3	1	2.061e-18	3.431e+0	0.31
S XVI	3.276	12	1	9.146e-19	2.165e+0	0.14
Ar XVII	3.140	7	1	6.604e-18	1.719e+0	1.00
Ar XVII	3.126	6	1	7.344e-19	1.719e+0	0.11
Ar XVII	3.124	5	1	1.018e-18	1.719e+0	0.15
S XVI	3.107	7	1	3.126e-18	2.165e+0	0.47
S XVI	3.106	6	1	1.584e-18	2.165e+0	0.24
Ar XVII	3.104	2	1	2.575e-18	1.719e+0	0.39
S XV	3.101	37	1	7.252e-19	1.366e+0	0.11
S XV	3.033	23	1	1.556e-18	1.366e+0	0.24

Table 2.8: List of astrophysical lines at 3-4 keV expected in our model. Basic line parameters such as energy, type of ion, type of transition – are taken from AtomDB database. Only the strongest lines are shown. Close lines of the same ion are grouped with horizontal lines.

II. The Burkert (BURK) profile (Burkert, 1995) has been shown to be successful in

explaining the kinematics of disk systems (e.g. Gentile et al., 2004):

$$\rho_{\rm BURK}(r) = \frac{\rho_B r_B^3}{(r_B + r)(r_B^2 + r^2)}. \tag{2.4}$$

III. Another common parametrizations of cored profiles are given by the pseudo-isothermal (ISO) profile (Kent, 1986)

$$\rho_{\rm ISO}(r) = \frac{\rho_c}{1 + r^2/r_c^2}. \tag{2.5}$$

IV. The profile found by Moore et al. (1999) from simulations is described by:

$$\rho_{\rm MOORE}(r) = \frac{\rho_c}{\sqrt{r/r_s}(1 + \sqrt{r/r_s})} \tag{2.6}$$

V. Binney & Evans (2001) found a profile from lensing data of the MW with the following general shape (BE in the following):

$$\rho_{\rm BE}(r) = \frac{\rho_c}{(r/r_s)(1 + (r/r_s))^{2.7}} \tag{2.7}$$

Because we reside in the inner part of Milky Way dark matter halo, it is the only object whose dark matter decay signal would be spread across the whole sky. The dark matter column density for the Milky Way halo can be calculated using the expression (Boyarsky et al., 2007b)

$$S_{DM}^{MW}(\phi) = \int_0^\infty \rho_{DM}\left(r(z,\phi)\right) dz \tag{2.8}$$

where $r(z,\phi) = \sqrt{r_\odot^2 + z^2 - 2zr_\odot \cos\phi}$ is the distance from the galactic center with z the distance along the line of sight and ϕ the angle away from the GC for an observer at earth (itself at $r_\odot$ from the GC). Expressed in galactic coordinates (l, b)

$$\cos\phi = \cos b \cos l. \tag{2.9}$$

It can be seen (e.g., Boyarsky et al., 2006c, 2008b, 2007b) that the function S_{DM}^{MW} can change only by a factor of few, when moving from the Galactic center ($\phi = 0^\circ$) to the anti-center ($\phi = 180^\circ$). That is, the Milky Way contribution to the decay is an all-sky signal.

The flux received at earth produced by dark matter decaying inside the cone of view, we can approximate by

$$F_{DM}^{FoV} = S_{DM}^{MW}(\phi)\Omega\Gamma/4\pi \tag{2.10}$$

in photons s^{-1} cm^{-2}, with Ω the size of the field of view in sr, Γ the decay width and the 4π to complete the distance modulus (the distance is already included in the Ω).

The exact solution, taking into account the varying density over the field of view, is

$$F_{DM}^{FoV} = \Sigma_{DM}^{FoV}\Gamma/4\pi \tag{2.11}$$

$$\Sigma_{DM}^{FoV} = 2\pi \int_{\phi=0}^{\phi=\omega} \int_{z=o}^{z=\infty} \frac{\rho(r(z,\phi))}{z^2} z^2 \sin(\phi) d\phi dz \tag{2.12}$$

for a circular field of view centered on the GC, with a radius of ω.

The mass modeling of the Milky Way is continuously updated and improved (see e.g., Nesti & Salucci, 2013; Deason et al., 2012; Bernal & Palomares-Ruiz, 2012; McMillan, 2011; Sofue et al., 2009; Xue et al., 2008; Smith et al., 2007; Battaglia et al., 2006; Alcock et al., 1996; Merrifield, 1992; Weber & de Boer, 2010). In Table 2.9 we summarize recent results. We are interested in predicting the flux from dark matter decay based on the dark matter content. Therefore, using the DM distributions in the MW as reported in this table, we compute Σ_{DM}^{FoV} for the galactic center and blank sky observations. In the galactic center case, we perform the integral in eq. 2.12 for $\omega = 14'$, and then correct the results for detector gaps with the ratio of the exposure-weighted average FoV size (corrected for detector gaps) to the size of an ideal 14' FoV. For the blank sky dataset, we computed $S_{DM}^{MW}\,\Omega$ (see eq. 2.8) for each blank sky pointing (each with its own ϕ), therefore assuming that so far away from the GC the DM density does not vary appreciably over the FoV, and take the exposure and FoV weighted average of all those pointings. It is then, just like the case for the GC, corrected for detector gaps.

Regarding the mass modeling of the Galactic Center, there are additional complications. Firstly, even tough according to Donato et al. (2009) and Gentile et al. (2009), the central surface densities of spiral galaxies are comparable, our field-of-view is only 14' in radius which translates to a physical scale of order 30 pc at the center of the halo, which is much smaller than one scale length. It is unfortunately not possible to observationally determine the DM distribution of the Milky Way within about 3 kpc from the halo center. Secondly, at these small scales, baryons dominate the mass budget and baryon physics may play an important role in shaping the DM distribution, in addition to possible warm dark matter effects. However, the extent of the influence of the processes is not well known. Thirdly, the central 3 kpc of the NFW distributions in Table 2.9 contribute between roughly 80% (least concentrated) to 90% (most concentrated) of the total Σ_{DM}^{FoV} for the GC observations. Therefore the best we can do is extrapolate profiles measured at larger radii down to the lower radii. We remain agnostic about the very central DM distribution and assume that uncertainty is enclosed within the spread in the different types of profiles that we already examined.

Recently, Lovell et al. (2015) analysed the high-resolution Aquarius simulations specifically in order to predict dark matter decay fluxes. Milky Way and Andromeda-like halos from these simulations were selected, and the fluxes determined based on the exposure times and position angles as used in this work and in Boyarsky et al. (2014a). Since the flux in this case is determined solely from the mass inside the field-of-view and the assumed DM particle lifetime, flux and projected mass are interchangeble in this study. This produced a range of fluxes that are in agreement with our projected mass brackets for the GC, and the flux ratios of the GC to M31, and GC to blank-sky. The confidence ranges from Lovell et al. (2015) are tighter than our literature-brackets, therefore we retain the latter in all joint analyses.

To round of this discussion about the dark matter masses, we shortly touch upon the dark matter content of Perseus and Andromeda in order to compare our observations in Figure 2 of our paper. As for the Milky Way, we compile available literature profiles of these objects and use those to determine the total dark matter mass present in the field of view of our observations (Boyarsky et al., 2014a). This is a more straightforward calculation as the physical size of these objects is much smaller than their distance to

Authors	Profile	$r_\odot$ kpc	r_* kpc	ρ_* $10^6 M_\odot/kpc^3$	$\Sigma^{FoV}_{DM,GC}$ $10^{-3} M_\odot/pc^2$	$\Sigma^{FoV}_{DM,BS}$ $10^{-3} M_\odot/pc^2$	GC/BS ratio
Smith et al. (2007)[a]	NFW	8	$25.2^{+6.2}_{-3.8}$	$10.6^{+1.5}_{-1.8}$	$142.6^{+33.3}_{-21.6}$	$5.6^{+1.8}_{-1.1}$	$25.6^{+13.9}_{-9.1}$
	NFW	8	$1.4^{+1.2}_{-0.5}$	$39.6^{+4.5}_{-3.2}$	$35.2^{+11.6}_{-5.7}$	$3.5^{+1.0}_{-0.5}$	$9.9^{+5.5}_{-3.4}$
Weber & de Boer (2010)	NFW[b]	8.33	$20.4^{+17.11}_{-6.4}$	$10.8^{+3.4}_{-3.4}$	$118.0^{+11.0}_{-4.0}$	$4.5^{+0.4}_{-0.4}$	$26.1^{+5.4}_{-3.1}$
	NFW[b]	8.33	$6.32^{+1.26}_{-0.78}$	$25.2^{+4.6}_{-4.6}$	$95.1^{+2.6}_{-2.2}$	$7.1^{+0.6}_{-0.6}$	$13.3^{+1.6}_{-1.3}$
	BE	8.33	$6.58^{+1.3}_{1.3}$	10.2	$22.0^{+3.5}_{-3.5}$	$4.0^{+0.8}_{-0.8}$	$5.5^{+2.4}_{-1.6}$
	Moore[c]	8.33	$6.58^{+1.3}_{1.3}$	30	$306.3^{+60.7}_{-60.7}$	$4.0^{+0.8}_{-0.8}$	$77.5^{+38.2}_{-25.6}$
	PISO[d]	8.33	$5.264^{+1.04}_{1.04}$	5	$11.4^{+2.6}_{-1.8}$	$3.7^{+0.7}_{-0.7}$	$3.1^{+1.7}_{-0.9}$
Battaglia et al. (2005)[e]	NFW	8	11.4	$14.86^{+0.71}_{-0.49}$	$95.1^{+5.3}_{-3.5}$	$5.0^{+0.5}_{-0.3}$	$19.0^{+2.4}_{-2.3}$
&Battaglia et al. (2006)	NFW	8	11.4	$16.12^{+0.44}_{-0.46}$	$103.9^{+3.5}_{-3.5}$	$5.9^{+0.3}_{-0.3}$	$17.7^{+1.6}_{-1.4}$
McMillan (2011)	NFW	8.29	$10.4^{+4.57}_{-2.3}$	$18^{+4.3}_{-4.3}$	$107.4^{+3.1}_{-0.4}$	$6.4^{+0.5}_{-0.5}$	$16.8^{+1.9}_{-1.3}$
Nesti & Salucci (2013)	NFW	8.08±0.2	$13.8^{+20.7}_{-6.6}$	$16.1^{+12.2}_{-5.6}$	$125.9^{+75.6}_{-26.1}$	$7.0^{+3.6}_{-1.3}$	$18.0^{+17.3}_{-8.5}$
	BURK	7.94±0.3	$4.13^{+4.4}_{-1.1}$	$9.26^{+4.0}_{-3.0}$	$22.9^{+42.8}_{-10.1}$	$7.3^{+23.1}_{-4.3}$	$3.2^{+18.9}_{-2.7}$
Xue et al. (2008)[f]	NFW	8	$4.2^{+0.3}_{-0.3}$	$21.9^{+-1}_{1.4}$	$54.6^{+7.0}_{-6.2}$	$3.8^{+0.7}_{-0.5}$	$14.4^{+4.5}_{-3.6}$
	NFW	8	$4.4^{+0.2}_{-0.4}$	$20.8^{+1.1}_{-1}$	$52.8^{+7.0}_{-6.2}$	$3.6^{+0.6}_{-0.6}$	$14.6^{+5.1}_{-3.5}$
	NFW[g]	8	$0.9^{+0.85}_{-0.36}$	$41.1^{+8.3}_{-5.8}$	$25.5^{+12.3}_{-8.8}$	$2.6^{+1.0}_{-0.7}$	$9.8^{+9.9}_{-5.1}$
	NFW[g]	8	$0.47^{+0.32}_{-0.18}$	$60.2^{+7.2}_{-7.2}$	$18.5^{+8.8}_{-5.3}$	$2.3^{+0.9}_{-0.6}$	$8.1^{+7.9}_{-3.9}$

Table 2.9: Overview of dark matter distributions as determined in the literature. r_* and ρ_* refer to the relevant characteristic radius and density for that particular type of profile. Where the profile was given in a different parametrization of the same profile (for example, concentration and virial mass), the values have been converted to r_* and ρ_*. The errors given are 1σ, which are naively converted from the error range given in that work if that range was not 1σ. $\Sigma^{FoV}_{DM,GC}$ (see Eq. 2.12) is the integral over the density of the galactic center inside the field of view of our observations, divided by the distance squared to each infinitesimal mass. $\Sigma^{FoV}_{DM,BS}$ is the same, but for the blank-sky dataset from Boyarsky et al. 2014. The errors on these projected mass densities are either 0.5σ to account for the degeneracy between the 2 parameters of the DM distribution, or 1σ if the fit from that study fixed one of those parameters (for example using a scaling relation between c and M_{vir}). *a)* the two descriptions are using different baryonic disks. *b)* some baryonic parameters are fixed in the fits. These two NFW's are the two extremes with reasonably good fits. *c)* the Moore model is very cuspy by design. *d)* the pseudo-isothermal sphere has an almost flat profile in the center. *e)* the second NFW takes anisotropy into account, and is a better fit that the first. *f)* analysis calibrated on two different simulations. *g)* includes an adiabatic correction.

us. We compute the enclosed projected mass of these literature profiles within the field of view (corrected for detector gaps), weighting by the exposure time of the different exposures, and then divide by the distance to the object squared to arrive at $\Sigma^{Perseus}_{DM}$ and Σ^{M31}_{DM}. For Perseus, we consider the profiles as determined by Reiprich & Boehringer (2002); Chen et al. (2007); Simionescu et al. (2012b); Storm et al. (2013); Ettori et al. (2002); Wojtak & Łokas (2007), and those by Klypin et al. (2002); Geehan et al. (2006); Widrow & Dubinski (2005); Seigar et al. (2008); Tempel et al. (2007); Chemin et al. (2009); Corbelli et al. (2010) for Andromeda.

2.3.5 Ion Abundances and Emission Lines

The Galactic Center is an object with a complicated signature in the X-rays. As Muno et al. (2004) show, not only does the GC show multi-temperature components in the X-ray spectra, these components also vary quite dramatically spatially over the field-of-view of Chandra, which is about half as large as that of XMM-Newton. The low temperature component as measured by Muno et al. (2004) typically has values of $0.7 - 0.9$ keV, while

the high temperature component can be as hot as 6 – 9 keV. The spatial variations in the elemental abundances of Si, S, Ar and Ca are reported to be as high as a factor 2 or 3, with only Fe having a reasonable homogeneous distribution. Our integrated spectrum of the entire inner 14' of the GC therefore will be a superposition of all these components, complicating our analysis significantly.

Restricting our modelling to the cleaner parts of the spectrum, 2.8–6.0 keV, we could find a reasonable fit using a single-temperature `vvapec` component with the elemental lines added manually as gaussians, and a folded powerlaw to account for non-thermal emission. No satisfactory two-temperature fits were found for temperatures in the range given by Muno et al. (2004), even when extending the energy range of our analysis[8]. We did not consider more than two temperature components, because it introduces too many degeneracies.

As mentioned, the emission lines from heavy ions are added by hand. We start with the strongest lines known (see Table 2.8), and work our way down so long as the fit requires it. As mentioned, the line detected at 3.539 keV might be influenced by the Ar XVII complex at 3.685 keV and the K XVIII lines at 3.515 and 3.47 keV. To explain the 3.539 keV line with Ar XVII, the width of this line should be much larger (95 – 130 eV) than what can be expected from the instrumental response based on simulations of this Ar complex. In addition, the flux in this Ar XVII complex would be higher than that of the same ion at 3.13 keV, which should not be possible based on the atomic data in Table 2.8.

For the K XVIII lines, it is unfortunately not possible to constrain their contribution to the 3.539 keV line in the same way as for Ar XVII, since we do not have other, stronger, detected lines of the same ion in our spectrum. In this case, one may attempt to predict the ratio of K XVIII flux to the fluxes of ions of other elements such as Ar XVII, Ca XIX, Ca XX, S XVI, etc. based on temperature and relative abundances. Since the GC emission consists of many different temperature and abundance components, it should be necessary to compute an estimate of the K XVIII flux for many different combinations of temperature and abundance. Based on the flux of each of the different detected strong lines in turn and assuming solar abundance (similarly to the analysis of Section 4 of Bulbul et al. (2014a)), the predictions for the K XVII flux can vary by more than an order of magnitude. Even without considering deviations from solar abundance (which may be as large as a factor 3 (Jeltema & Profumo, 2015)), the detected flux in the 3.539 keV line falls within these predictions for a respectable fraction of these physically plausible scenarios. It is therefore not possible *based on the GC data alone* to exclude the astrophysical origin of this 3.539 keV line in the GC.

[8]The two-temperature fit can be made satisfactory e.g. by adding 1.2% systematic error in quadrature – a value much larger than the typical systematic errors for line-like uncertainties ($\sim$0.5%, see Sec. 5 of Iakubovskyi (2013) for details). When adding such large errors, the `vvapec` temperatures become consistent with previous works (e.g. Muno et al. (2004)) and the abundances of S, Ar, Ca and K are 0.8-1.2, 1.2-1.8, 1.6-2.4 and 0.3-3.4 Solar values at 68% level, respectively, in full accordance with (Jeltema & Profumo, 2015).

2.4 Literature Response

BASED ON

Comment on the paper "Dark matter searches going bananas: the contribution of Potassium (and Chlorine) to the 3.5 keV line" by T. Jeltema and S. Profumo
Alexey Boyarsky, Jeroen Franse, Dmytro Iakubovskyi, Oleg Ruchayskiy
Published on *arXiv*

In response to Boyarsky et al. (2014a) and Bulbul et al. (2014a), the authors of Jeltema & Profumo (2015) have argued that if one restricts the modeling of the emission of the central part of M31 to the energy range $3-4$ keV, and uses a single `powerlaw` as a model of the continuum, the significance of the detection of the line at 3.53 keV in the spectrum of M31 drops below 2σ. They also argued that when one ignores the detection in M31, the line in the spectra of the galaxy clusters and of the Galactic Center can be explained by an atomic transition in the K XVIII ion, provided one also assumes both an abundance of K XVIII and a set of physical conditions in these objects that are hard to exclude.

In this Section we show that restricting the analysis of the M31 spectrum to $3-4$ keV is not justified. The continuum is well modelled by a power law model up to 8 keV and the parameters of this model are well constrained at this wider interval. Limiting the analysis to $3-4$ keV only results in increased uncertainty and, although the flux in the 3.53 keV line is consistent with the one reported in (Boyarsky et al., 2014a), the significance of its detection is naturally smaller on the $3-4$ keV than on the whole $2-8$ keV interval, where the astrophysical background is better constrained. We also argue that with the M31 data included, the interpretation of the 3.53 keV line as a K XVIII line in several studied objects together is problematic.

We start by repeating the analysis of (Jeltema & Profumo, 2015): we fit the M31 spectrum over the interval 3–4 keV with a single `powerlaw` (in order to avoid having to model the instrumental background, we subtract it from our spectra.)[9] The fit is good ($\chi^2 = 22.4$ for 27 d.o.f.).[10] The parameters of the `powerlaw` are: PL index 1.65 ± 0.05 (3% relative error), and PL norm $(1.19 \pm 0.07) \times 10^{-3}\,\mathrm{cts/sec/cm^2/keV}$ at 3.5 keV (the relative error being 6.3%). An additional line is detected against this continuum at energy 3.53 keV and with normalization $(2.7 \pm 1.5) \times 10^{-6}\,\mathrm{cts/sec/cm^2}$ (less than 2σ significance, $\Delta\chi^2 = 3.4$ when adding this line). Thus, we have reproduced both the flux and the significance reported in (Jeltema & Profumo, 2015).

However, once we extend the powerlaw obtained over the interval $3-4$ keV to higher energies, we see that it *significantly overpredicts* the count rate in all energy bins above 4 keV as Fig. 2.12 demonstrates.

Let us now compare this result with the fit over the whole interval 2–8 keV (as in Ref. (Boyarsky et al., 2014a)). The wider range of energies allows us to determine the parameters of the `powerlaw` with better precision: PL index 1.71 ± 0.01 (0.5% relative error), PL norm = $(1.18 \pm 0.01) \times 10^{-3}\,\mathrm{cts/sec/cm^2/keV}$ at 3.5 keV (0.7% relative

[9] The spectral modeling has been performed with the X-Ray Spectral Fitting Package `Xspec` (Arnaud, 1996) v.12.8.0.

[10] Unlike (Jeltema & Profumo, 2015) we have binned the spectrum by 60 eV (as in (Boyarsky et al., 2014a)) to make bins roughly statistically independent. We verified that our conclusion does not change for finer binning.

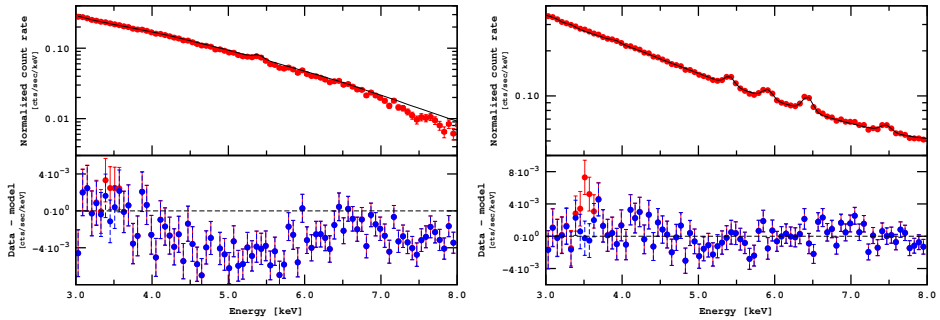

Figure 2.12: *Left panel:* Best fit powerlaw, as determined over the 3–4 keV interval in (Jeltema & Profumo, 2015), extended to higher energies. Such a powerlaw significantly overpredicts the count rate in all bins at $E > 4$ keV. A wide group of near-zero residuals around 6.5 keV corresponds to the complex of lines of iron and other elements (unmodeled). *Right panel:* The data over a wider range of energies processed and fitted in (Boyarsky et al., 2014a)) with the line at 3.53 keV unmodeled. Other lines in the range $3-4$ keV are included in the model.

error). The improvement of the quality of fit when adding the line around 3.53 keV was $\Delta\chi^2 = 13$ (which is about 3σ for 2 degrees of freedom: position and normalization of the line). This is the most significant feature in the 3–4 keV range. In Table 2.10 we list all the lines detected in the interval 3–4 keV with significance more than 1σ. Unlike the results of (Jeltema & Profumo, 2015) (see Fig. 3 therein), the lines at 3.91 keV (complex of Ca XIX and Ar XVII lines) have also been detected in this case with the significance above 2σ. In the case of the fit over the $3-4$ keV range, these lines were partially compensated by the `powerlaw` continuum. In addition, the parameters of the continuum as determined over the narrow range of energies naturally suffer from larger errors (around $3-6\%$ for the fit over $3-4$ keV interval vs. $0.5-0.7\%$ for the fit of (Boyarsky et al., 2014a)). As the flux in the line in question is about 4% of the continuum at these energies, the parameters of the background model should be determined with a precision greater than that in order to reliably detect such a weak line. This explains the reduced best-fit flux and the diminished significance of the line at 3.53 keV.

Finally, we make the observation that complexes of argon, calcium and sulphur at energies 3.14 keV, 3.37 keV and 3.91 keV (of which only the 3.91 keV complex is detected at more than 2σ) have fluxes *lower* than that of the unidentified spectral feature at 3.53 keV. This *challenges* the interpretation of the feature as a K XVIII complex. Indeed,

Line	Position, keV	Flux, ph/sec/cm^2
Ar XVII/S XV	3.14 ± 0.04	$2.3 \pm 1.4 \times 10^{-6}$
Ar XVIII/S XVI/Cl XVI	3.37 ± 0.03	$3.6 \pm 1.4 \times 10^{-6}$
Ar XVII/Ca XIX	3.91 ± 0.02	$4.3 \pm 1.3 \times 10^{-6}$
DM line candidate	3.53 ± 0.03	$4.9^{+1.6}_{-1.3} \times 10^{-6}$

Table 2.10: Position and flux of lines found in the central part of M31 (Boyarsky et al., 2014a), together with 1σ error ranges.

according to AtomDB v2.0.2 (Foster et al., 2011) K XVIII emissivity is at least an order of magnitude lower than emissivities of the complexes in the intervals $3.85 - 3.95$ keV and $3.08 - 3.18$ keV (see Fig. 2.13 based on the data from (Foster et al., 2011)). This relation between emissivities is based on the assumption of solar abundances for these elements. To change this conclusion a strongly super-solar abundance of K XVIII would be required.

In conclusion: the line 3.53 keV is detected at $\sim 3\sigma$ level in the spectrum of the Andromeda galaxy against a background model with the continuum component constrained at the 2–8 keV interval as in (Boyarsky et al., 2014a). Fitting the data in the much narrower $3 - 4$ keV range reduces the significance of the detection as the sensitivity likewise reduces with less data, however this does not contradict the flux in the line detected in (Boyarsky et al., 2014a). The fit over the narrow interval of energies, as performed in (Jeltema & Profumo, 2015), provides a best fit value of the slope of the power law background that systematically over-predicts the value of the flux above 4 keV, and is therefore significantly ruled out by the whole spectrum.

The observation of the line at 3.53 keV in the center of M31 is in stark contradiction with its interpretation as a K XVIII atomic transition – it would require an extremely super-solar abundance of K XVIII *and* a super-solar ratio of abundance of K XVIII relative to AR XVII and CA XIX. The presence of this line in different types of objects – galaxy clusters, M31, and the Galactic Center – makes it challenging to explain all these signals together by emission from K XVIII, even if this interpretation is hard to exclude from the GC data only.

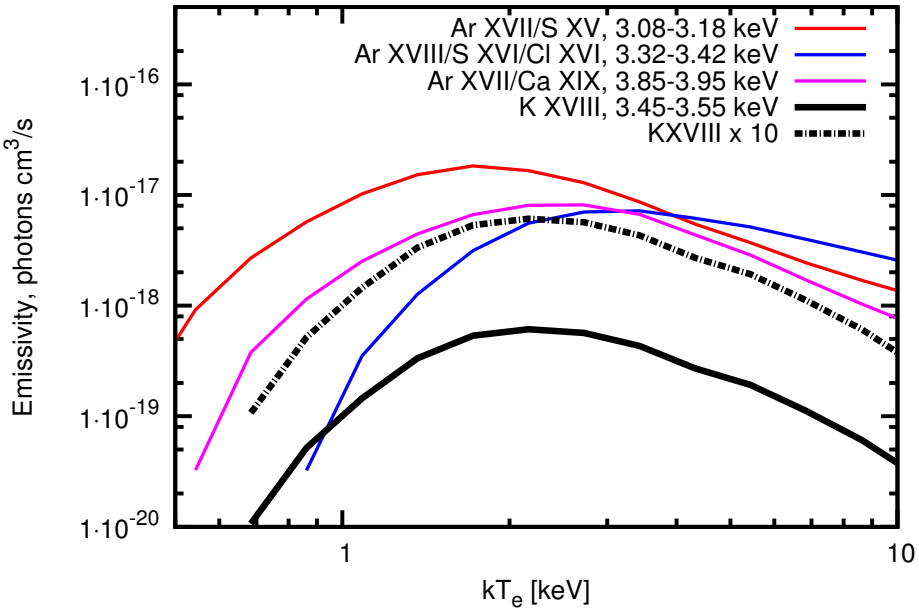

Figure 2.13: Emissivities of different line complexes as a function of plasma temperature (assuming solar abundances of all elements). The emissivity of the K XVIII line complex near 3.5 keV is at least an order of magnitude below those of the other complexes. The data is from AtomDB v2.0.2 (Foster et al., 2011).